

Learned convex regularizers for inverse problems

Subhadip Mukherjee[†], Sören Dittmer[‡], Zakhar Shumaylov[†], Sebastian Lunz[†], Ozan Öktem^{*}, and Carola-Bibiane Schönlieb[†]

Abstract—We consider the variational reconstruction framework for inverse problems and propose to learn a data-adaptive input-convex neural network (ICNN) as the regularization functional. The ICNN-based convex regularizer is trained adversarially to discern ground-truth images from unregularized reconstructions. Convexity of the regularizer is attractive since (i) one can establish analytical convergence guarantees for the corresponding variational reconstruction problem and (ii) devise efficient and provable algorithms for reconstruction. In particular, we show that the optimal solution to the variational problem converges to the ground-truth if the penalty parameter decays sub-linearly with respect to the norm of the noise. Further, we prove the existence of a subgradient-based algorithm that leads to monotonically decreasing error in the parameter space with iterations. To demonstrate the performance of our approach for solving inverse problems, we consider the tasks of deblurring natural images and reconstructing images in computed tomography (CT), and show that the proposed convex regularizer is at least competitive with and sometimes superior to state-of-the-art data-driven techniques for inverse problems.

Index Terms—Inverse problems, data-driven convex regularization, adversarial learning.

I. INTRODUCTION

INVERSE problems arise in numerous scientific applications, e.g., in virtually every modern medical imaging modality, wherein the key objective is to estimate some parameters of interest based on an indirect and possibly noisy measurement.

An inverse problem is said to be ill-posed if it has no or multiple solutions, or if its solution is not continuous in the measurement. Any traditional approaches attempt to alleviate the issue of ill-posedness by involving handcrafted prior information on possible reconstructions.

While such analytical priors usually lead to provable properties, they fall short in terms of data-adaptability; that is, it is impossible to define formally, which, of all possible images, are *natural images*. In recent years, several solutions to this problem emerged with the rise of deep learning methods [1]. While the deep learning-based techniques often produce reconstructions of astonishing quality, they typically lack many, if not all, of the provable properties that analytical methods offer. In this work, we propose an approach that integrates deep learning into the classical regularization theory, by learning a strongly convex regularizer to incorporate prior information into a variational reconstruction setting.

Before explaining our contributions in more detail, we give a brief overview of related works.

[†]: Department of Applied Mathematics and Theoretical Physics, University of Cambridge, UK; emails: {sm2467, zs334, sl767, cbs31}@cam.ac.uk. [‡]: Center for Industrial Mathematics, University of Bremen, Germany; email: sdittmer@math.uni-bremen.de. ^{*}: Department of Mathematics, KTH – Royal Institute of Technology, Sweden; email: ozan@kth.se.

A. Related works

One of the most widely used data-driven approaches for inverse problems consists in *unrolling* of iterative model-based methods [2], [3]. Iterative unrolling techniques are supervised and incorporate the forward operator in the learning model to achieve data-efficiency. Another common practice is to regularize the variational problem using an appropriately pre-trained neural network.

Aside from [4], the idea of using a trained neural network as a regularizer was considered in [5] (referred to as NETT). The key difference between the AR and the NETT approach lies in the training protocol for the regularizer. While the AR is trained with an objective to discriminate desired images from noisy ones, the NETT regularizer rests upon an encoder-decoder setup. In both cases, gradient-descent is used for solving the variational reconstruction problem, and no convergence guarantees for it can be given. In this work, we leverage strong convexity by generalizing the parametrization of input-convex neural networks (ICNNs) proposed in [6] while designing the regularizer. This not only allows us to show well-posedness and strong convergence of the variational reconstruction but also guides the development of a convergent sub-gradient descent algorithm for reconstruction. Further, since a penalty term may be interpreted as the inclusion of prior information, the idea of incorporating the prior knowledge by restricting the reconstruction to lie in the range of a generative model proposed in [7] is also closely related to our work. Under smoothness conditions, this approach can be shown to be equivalent to learning a penalty function via a Lagrangian argument [8].

B. Specific contributions

This work builds upon [4] that introduced the adversarial regularizer (AR) framework. The idea in AR is to replace a handcrafted regularizer with a learned one in a variational scheme for solving an ill-posed inverse problem.

By utilizing ICNNs [6], one can rigorously study regularizing properties of such variational schemes even when the regularizer is learned. The convergence guarantees and ICNN parametrization developed by us are applicable in the general setting where the underlying parameters and the measurement belong to Hilbert spaces. The resulting data-driven adversarial convex regularizer (ACR) offers reconstruction performance that is competitive with similar learned methods while being provably convergent simultaneously. In specific applications, we found that a convex regularizer even outperforms its non-convex variant, especially when the training dataset is small, and the forward operator is highly ill-conditioned.

C. Notations

We denote spaces by blackboard-bold letters (e.g. \mathbb{X}) and functionals by calligraphic letters (e.g. \mathcal{R}). Generic elements of a space are denoted by boldface lowercase letters (e.g. $\mathbf{x} \in \mathbb{X}$). Simple uppercase letters are used to denote random variables, e.g., a generic \mathbb{X} -valued random variable is denoted as X , with its distribution being π_X .

D. Mathematical background on inverse problems

Inverse problems deal with reconstructing unknown model parameter $\mathbf{x}^* \in \mathbb{X}$ from the indirect measurement

$$\mathbf{y}^\delta = \mathcal{A}(\mathbf{x}^*) + \mathbf{e} \in \mathbb{Y}, \quad (1)$$

where $\mathcal{A} : \mathbb{X} \rightarrow \mathbb{Y}$ is the forward operator and $\mathbf{e} \in \mathbb{Y}$, $\|\mathbf{e}\|_2 \leq \delta$, denotes measurement noise. Here \mathbb{X} and \mathbb{Y} are Hilbert spaces containing possible model parameters and data, respectively.

In the context of medical imaging, e.g., computed tomography (CT), the model parameter $\mathbf{x}^* \in \mathbb{X}$ is the image of the interior structure one seeks to recover. The measurement $\mathbf{y}^\delta \in \mathbb{Y}$ (*data*) represents indirect observations of \mathbf{x}^* .

In the classical function-analytic formulation, \mathbf{x}^* is modeled as deterministic and the standard practice is to approximate it from \mathbf{y}^δ by solving a variational reconstruction problem:

$$\min_{\mathbf{x} \in \mathbb{X}} \mathcal{L}_{\mathbb{Y}}(\mathbf{y}^\delta, \mathcal{A}(\mathbf{x})) + \alpha \mathcal{R}(\mathbf{x}). \quad (2)$$

The loss functional $\mathcal{L}_{\mathbb{Y}} : \mathbb{Y} \times \mathbb{Y} \rightarrow \mathbb{R}$ provides a measure of data-fidelity and is typically chosen based on the statistical properties of the measurement noise \mathbf{e} , whereas the regularization functional $\mathcal{R} : \mathbb{X} \rightarrow \mathbb{R}$ penalizes undesirable images. The penalty parameter $\alpha > 0$ trades-off data-fidelity with the regularization penalty and is chosen depending on the noise strength. In the subsequent part, we consider the squared- ℓ_2 loss to measure data-fidelity, i.e., $\mathcal{L}_{\mathbb{Y}}(\mathbf{y}_1, \mathbf{y}_2) = \|\mathbf{y}_1 - \mathbf{y}_2\|_{\mathbb{Y}}^2$, unless otherwise specified, and correspondingly, (2) reduces to

$$\min_{\mathbf{x} \in \mathbb{X}} \|\mathbf{y}^\delta - \mathcal{A}(\mathbf{x})\|_{\mathbb{Y}}^2 + \alpha \mathcal{R}(\mathbf{x}). \quad (3)$$

In the statistical formulation of inverse problems, one models the data as a single sample \mathbf{y}^δ of the \mathbb{Y} -valued random variable

$$Y = \mathcal{A}(X) + \mathbf{e}, \quad (4)$$

and aims to estimate the posterior distribution of X conditioned on $Y = \mathbf{y}^\delta$, denoted as $\pi_{\text{post}}(X = \mathbf{x}|Y = \mathbf{y}^\delta)$. Using the Bayes rule, the posterior distribution can be expressed in terms of the data-likelihood and the prior:

$$\pi_{\text{post}}(X = \mathbf{x}|Y = \mathbf{y}^\delta) = \frac{\pi_{\text{data}}(Y = \mathbf{y}^\delta|X = \mathbf{x})\pi_X(X = \mathbf{x})}{Z(\mathbf{y}^\delta)}, \quad (5)$$

where $Z(\mathbf{y}^\delta)$ is a normalizing constant independent of \mathbf{x} . While the data-likelihood is known in most inverse problems, the prior, which encodes a-priori belief about \mathbf{x} , is typically unknown. In the sequel, we write $\pi_{\text{post}}(X = \mathbf{x}|Y = \mathbf{y}^\delta)$ as $\pi_{\text{post}}(\mathbf{x}|\mathbf{y}^\delta)$, and likewise for the other probability measures in (5) for simplicity. An approximation of the true image is typically obtained by summarizing the posterior distribution into a point-estimate, such as the mean. Among many choices available for extracting

a point-estimate from the posterior, a particularly popular one is to compute its *mode*, leading to the so-called *maximum a-posteriori probability* (MAP) estimate:

$$\min_{\mathbf{x} \in \mathbb{X}} -\log \pi_{\text{data}}(\mathbf{y}^\delta|\mathbf{x}) - \log \pi_X(\mathbf{x}). \quad (6)$$

When $\pi_X(\mathbf{x}) \propto \exp(-\lambda \mathcal{R}(\mathbf{x}))$, the MAP estimation problem (6) is essentially equivalent to the variational reconstruction framework (2) in the classical setting.

II. THEORETICAL RESULTS

In this section, we will first construct a convex regularizer and prove convergence of the minimizer of the resulting variational loss to the ground-truth. Subsequently, we develop a parametrization strategy using a neural network that achieves the properties required for convergence and explain the training protocol we adopt.

A. Properties of strongly-convex regularizers

First, we begin by investigating the analytical properties of a regularization functional of the form

$$\mathcal{R}(\mathbf{x}) = \mathcal{R}'(\mathbf{x}) + \rho_0 \|\mathbf{x}\|_{\mathbb{X}}^2, \quad (7)$$

where $\|\cdot\|_{\mathbb{X}}$ is the norm induced by the inner product structure of \mathbb{X} and $\mathcal{R}' : \mathbb{X} \rightarrow \mathbb{R}$ is 1-Lipschitz and convex in \mathbf{x} . No smoothness assumption is made on $\mathcal{R}'(\mathbf{x})$. The corresponding reconstruction problem consists in minimizing the variational objective $J_\alpha(\mathbf{x}; \mathbf{y}^\delta)$ with respect to \mathbf{x} , where

$$J_\alpha(\mathbf{x}; \mathbf{y}) := \|\mathbf{y} - \mathcal{A}(\mathbf{x})\|_{\mathbb{Y}}^2 + \alpha (\mathcal{R}'(\mathbf{x}) + \rho_0 \|\mathbf{x}\|_{\mathbb{X}}^2). \quad (8)$$

The forward operator is assumed to be bounded and linear, so its operator norm is bounded, i.e.,

$$\beta_1 := \sup_{\mathbf{x} \in \mathbb{X}} \frac{\|\mathcal{A}(\mathbf{x})\|_{\mathbb{Y}}}{\|\mathbf{x}\|_{\mathbb{X}}} < \infty.$$

In the following, we establish that $J_\alpha(\mathbf{x}; \mathbf{y})$ has a unique minimizer $\hat{\mathbf{x}}_\alpha(\mathbf{y})$, for any \mathbf{y} and $\alpha > 0$, varying continuously in \mathbf{y} . Moreover, for an appropriate choice of $\alpha(\delta)$, we show that $\hat{\mathbf{x}}_\alpha(\mathbf{y}^\delta)$ converges as $\delta \rightarrow 0$.

Proposition 1. *(Existence and uniqueness) $J_\alpha(\mathbf{x}; \mathbf{y})$ is strongly convex in \mathbf{x} with parameter $2\alpha\rho_0$ and has a unique minimizer $\hat{\mathbf{x}}_\alpha(\mathbf{y})$ for every \mathbf{y} and $\alpha > 0$. We also have*

$$J_\alpha(\mathbf{x}; \mathbf{y}) \geq J_\alpha(\hat{\mathbf{x}}_\alpha(\mathbf{y}); \mathbf{y}) + \alpha\rho_0 \|\mathbf{x} - \hat{\mathbf{x}}_\alpha(\mathbf{y})\|_{\mathbb{X}}^2, \quad (9)$$

for any $\mathbf{x} \in \mathbb{X}$.

Proof: It follows from the definition of strong convexity that $h_\mu(\mathbf{x}) = h(\mathbf{x}) + \frac{\mu}{2} \|\mathbf{x}\|_{\mathbb{X}}^2$ is μ -strongly convex when h is convex. Since $\|\mathbf{y} - \mathcal{A}(\mathbf{x})\|_{\mathbb{Y}}^2 + \alpha \mathcal{R}'(\mathbf{x})$ is convex, it follows that $J_\alpha(\mathbf{x}; \mathbf{y})$ is $2\alpha\rho_0$ -strongly convex in \mathbf{x} , and consequently, for any $\mathbf{x}, \mathbf{v} \in \mathbb{X}$, we have that

$$J_\alpha(\mathbf{x}; \mathbf{y}) \geq J_\alpha(\mathbf{v}; \mathbf{y}) + \langle (\mathbf{x} - \mathbf{v}), \mathbf{g}_\mathbf{v} \rangle + \alpha\rho_0 \|\mathbf{x} - \mathbf{v}\|_{\mathbb{X}}^2, \quad (10)$$

for all $\mathbf{g}_\mathbf{v} \in \partial J_\alpha(\mathbf{v}; \mathbf{y})$. In particular, when $\mathbf{v} = \hat{\mathbf{x}}$ is a minimizer of $J_\alpha(\cdot; \mathbf{y})$, we have $\mathbf{0} \in \partial J_\alpha(\mathbf{v}; \mathbf{y})$, and therefore (10) leads to

$$J_\alpha(\mathbf{x}; \mathbf{y}) \geq J_\alpha(\hat{\mathbf{x}}; \mathbf{y}) + \alpha\rho_0 \|\mathbf{x} - \hat{\mathbf{x}}\|_{\mathbb{X}}^2. \quad (11)$$

(11) also ascertains that if there are two minimizers $\hat{\mathbf{x}}_1$ and $\hat{\mathbf{x}}_2$, one must have $\hat{\mathbf{x}}_1 = \hat{\mathbf{x}}_2$, thereby guaranteeing uniqueness. The unique minimizer, denoted as $\hat{\mathbf{x}}_\alpha(\mathbf{y})$, satisfies (9). ■

Proposition 2. (Stability) The optimal solution $\hat{\mathbf{x}}_\alpha(\mathbf{y})$ is continuous in \mathbf{y} .

Proof: Denote a perturbation of magnitude δ_1 on \mathbf{y} as

$$\mathbf{y}^{\delta_1} = \mathbf{y} + \boldsymbol{\delta}_1, \text{ with } \|\boldsymbol{\delta}_1\|_{\mathbb{Y}} \leq \delta_1.$$

Define for any $\delta_1 > 0$

$$p_{\delta_1} := J_\alpha(\hat{\mathbf{x}}_\alpha(\mathbf{y}^{\delta_1}); \mathbf{y}) - J_\alpha(\hat{\mathbf{x}}_\alpha(\mathbf{y}^{\delta_1}); \mathbf{y}^{\delta_1}).$$

Clearly, $\lim_{\delta_1 \rightarrow 0} p_{\delta_1} = 0$ since $J_\alpha(\mathbf{x}; \mathbf{y})$ is continuous in \mathbf{y} for any $\mathbf{x} \in \mathbb{X}$. Further, p_{δ_1} can be expressed as

$$\begin{aligned} p_{\delta_1} &= [J_\alpha(\hat{\mathbf{x}}_\alpha(\mathbf{y}^{\delta_1}); \mathbf{y}) - J_\alpha(\hat{\mathbf{x}}_\alpha(\mathbf{y}); \mathbf{y})] \\ &+ [J_\alpha(\hat{\mathbf{x}}_\alpha(\mathbf{y}); \mathbf{y}) - J_\alpha(\hat{\mathbf{x}}_\alpha(\mathbf{y}); \mathbf{y}^{\delta_1})] \\ &+ [J_\alpha(\hat{\mathbf{x}}_\alpha(\mathbf{y}); \mathbf{y}^{\delta_1}) - J_\alpha(\hat{\mathbf{x}}_\alpha(\mathbf{y}^{\delta_1}); \mathbf{y}^{\delta_1})]. \end{aligned} \quad (12)$$

For convenience, denote the terms within square brackets in (12) as t_1 , t_2 , and t_3 , respectively. By Proposition 1,

$$t_1, t_3 \geq \alpha \rho_0 \|\mathbf{x}_\alpha(\mathbf{y}^{\delta_1}) - \mathbf{x}_\alpha(\mathbf{y})\|_{\mathbb{X}}^2,$$

and by continuity of $J_\alpha(\cdot; \mathbf{y})$ in \mathbf{y} , we have $\lim_{\delta_1 \rightarrow 0} t_2 = 0$. Therefore $\lim_{\delta_1 \rightarrow 0} (p_{\delta_1} - t_2) = 0$, and (12) implies that

$$p_{\delta_1} - t_2 = t_1 + t_3 \geq 2\alpha \rho_0 \|\hat{\mathbf{x}}_\alpha(\mathbf{y}^{\delta_1}) - \hat{\mathbf{x}}_\alpha(\mathbf{y})\|_{\mathbb{X}}^2. \quad (13)$$

Further, we have that

$$\begin{aligned} p_{\delta_1} - t_2 &= \|\mathcal{A}(\hat{\mathbf{x}}_\alpha(\mathbf{y}^{\delta_1})) - \mathbf{y}\|_{\mathbb{Y}}^2 - \|\mathcal{A}(\hat{\mathbf{x}}_\alpha(\mathbf{y}^{\delta_1})) - \mathbf{y}^{\delta_1}\|_{\mathbb{Y}}^2 \\ &+ \|\mathcal{A}(\hat{\mathbf{x}}_\alpha(\mathbf{y})) - \mathbf{y}^{\delta_1}\|_{\mathbb{Y}}^2 - \|\mathcal{A}(\hat{\mathbf{x}}_\alpha(\mathbf{y})) - \mathbf{y}\|_{\mathbb{Y}}^2. \end{aligned} \quad (14)$$

Now, substituting $\mathbf{y}^{\delta_1} = \mathbf{y} + \boldsymbol{\delta}_1$ in (14) and expanding further,

$$\begin{aligned} p_{\delta_1} - t_2 &= 2\langle \boldsymbol{\delta}_1, \mathcal{A}(\hat{\mathbf{x}}_\alpha(\mathbf{y}^{\delta_1})) \rangle - \|\boldsymbol{\delta}_1\|_{\mathbb{Y}}^2 \\ &- 2\langle \boldsymbol{\delta}_1, \mathcal{A}(\hat{\mathbf{x}}_\alpha(\mathbf{y})) \rangle + \|\boldsymbol{\delta}_1\|_{\mathbb{Y}}^2 \\ &= 2\langle \boldsymbol{\delta}_1, \mathcal{A}(\hat{\mathbf{x}}_\alpha(\mathbf{y}^{\delta_1}) - \hat{\mathbf{x}}_\alpha(\mathbf{y})) \rangle \\ &\leq 2\beta_1 \delta_1 \|\hat{\mathbf{x}}_\alpha(\mathbf{y}^{\delta_1}) - \hat{\mathbf{x}}_\alpha(\mathbf{y})\|_{\mathbb{X}}, \end{aligned} \quad (15)$$

where the last inequality in (15) is due to Cauchy-Schwarz. Finally, combining (13) with (15), we have

$$\|\hat{\mathbf{x}}_\alpha(\mathbf{y}^{\delta_1}) - \hat{\mathbf{x}}_\alpha(\mathbf{y})\|_{\mathbb{X}} \leq \frac{\beta_1 \delta_1}{\alpha \rho_0}. \quad (16)$$

(16) indicates that $\lim_{\delta_1 \rightarrow 0} \|\hat{\mathbf{x}}_\alpha(\mathbf{y}^{\delta_1}) - \hat{\mathbf{x}}_\alpha(\mathbf{y})\|_{\mathbb{X}} = 0$, confirming that $\hat{\mathbf{x}}_\alpha(\mathbf{y})$ is continuous in \mathbf{y} for a fixed α . ■

Proposition 3. (Convergence) For $\delta \rightarrow 0$ and $\alpha(\delta) \rightarrow 0$ such that $\frac{\delta}{\alpha(\delta)} \rightarrow 0$, we have that $\hat{\mathbf{x}}_\alpha(\mathbf{y}^\delta)$ converges to the \mathcal{R} -minimizing solution \mathbf{x}^\dagger given by

$$\mathbf{x}^\dagger = \arg \min_{\mathbf{x}} \mathcal{R}(\mathbf{x}) \text{ subject to } \mathcal{A}(\mathbf{x}) = \mathbf{y}^0, \quad (17)$$

where \mathbf{y}^0 is the clean data and $\|\mathbf{y}^\delta - \mathbf{y}^0\|_{\mathbb{Y}} \leq \delta$.

Proof: By (16), we have that

$$\|\hat{\mathbf{x}}_\alpha(\mathbf{y}^\delta) - \hat{\mathbf{x}}_\alpha(\mathbf{y}^0)\|_{\mathbb{X}} \leq \frac{\beta_1 \delta}{\alpha \rho_0}. \quad (18)$$

Since \mathcal{A} is linear and \mathcal{R} is strongly-convex, the solution \mathbf{x}^\dagger to (17) is unique and it can alternatively be expressed as

$$\begin{aligned} \mathbf{x}^\dagger &= \lim_{\alpha \rightarrow 0+} \left(\arg \min_{\mathbf{x}} \mathcal{R}(\mathbf{x}) + \frac{1}{\alpha} \|\mathcal{A}(\mathbf{x}) - \mathbf{y}^0\|_{\mathbb{Y}}^2 \right) \\ &= \lim_{\alpha \rightarrow 0+} \left(\arg \min_{\mathbf{x}} \alpha \mathcal{R}(\mathbf{x}) + \|\mathcal{A}(\mathbf{x}) - \mathbf{y}^0\|_{\mathbb{Y}}^2 \right) \\ &= \lim_{\alpha \rightarrow 0+} \hat{\mathbf{x}}_\alpha(\mathbf{y}^0). \end{aligned} \quad (19)$$

Let $\epsilon(\alpha) = \|\hat{\mathbf{x}}_\alpha(\mathbf{y}^0) - \mathbf{x}^\dagger\|_{\mathbb{X}}$. Then, by (19), $\lim_{\alpha \rightarrow 0} \epsilon(\alpha) = 0$. Thus, combining (18) and (19), and using the triangle inequality, one can argue that

$$\begin{aligned} \|\hat{\mathbf{x}}_\alpha(\mathbf{y}^\delta) - \mathbf{x}^\dagger\|_{\mathbb{X}} &\leq \|\hat{\mathbf{x}}_\alpha(\mathbf{y}^\delta) - \hat{\mathbf{x}}_\alpha(\mathbf{y}^0)\|_{\mathbb{X}} \\ &+ \|\hat{\mathbf{x}}_\alpha(\mathbf{y}^0) - \mathbf{x}^\dagger\|_{\mathbb{X}} \leq \frac{\beta_1 \delta}{\alpha \rho_0} + \epsilon(\alpha). \end{aligned}$$

Now, if $\lim_{\delta \rightarrow 0} \alpha(\delta) \rightarrow 0$ and $\lim_{\delta \rightarrow 0} \frac{\delta}{\alpha(\delta)} \rightarrow 0$, the inequality above implies that

$$\lim_{\delta \rightarrow 0} \|\hat{\mathbf{x}}_\alpha(\mathbf{y}^\delta) - \mathbf{x}^\dagger\|_{\mathbb{X}} = 0,$$

thus proving the proposition. ■

B. Input-convex neural networks

This section introduces ICNNs in the infinite dimensional setting. It is based on generalizing the construction in [6]. In particular, we need to implement the convex functional \mathcal{R}' in (7) on L^2 spaces, i.e., $\mathbb{X} = L^2$. Discretizing this parameterized operator coincides with the construction presented in [6]. More precisely, define the activation-spaces of our network to be $\mathbb{V}_i := L^2([0, 1]^{n_i})$ for $i = 0, \dots, L-1$, with $\mathbb{V}_0 = \mathbb{X}$ and $\mathbb{V}_L = \mathbb{R}$. We assume the input \mathbf{x} of our network to be in \mathbb{V}_0 and set $\mathbf{0} := \mathbf{z}_0 \in \mathbb{V}_0$. We then define the output of each layer $i = 0, \dots, L$ to be

$$\mathbf{z}_{i+1} = \varphi_i(\mathcal{B}_i \mathbf{z}_i(\mathbf{x}) + \mathcal{W}_i(\mathbf{x}) + \mathbf{b}_i). \quad (20)$$

Here $\mathcal{B}_i : \mathbb{V}_i \rightarrow \mathbb{V}_{i+1}$ and $\mathcal{W}_i : \mathbb{V}_0 \rightarrow \mathbb{V}_{i+1}$ are bounded integral operators and we assume the kernels of the \mathcal{B}_i 's to be pointwise non-negative. The $\varphi_i : \mathbb{V}_{i+1} \rightarrow \mathbb{V}_{i+1}$ are given by the pointwise application of a convex monotone function from \mathbb{R} to \mathbb{R} which, in an overload of notation, is also denoted by φ_i . Further let the biases, \mathbf{b}_i , be in \mathbb{V}_{i+1} . The output of the network $\mathcal{R}' : \mathbb{V}_0 \rightarrow \mathbb{R}$ we define to be the output of the last layer L , i.e., $\mathcal{R}'(\mathbf{x}) := \mathbf{z}_L(\mathbf{x})$.

The convexity of \mathcal{R}' in \mathbf{x} follows analogously to the finite-dimensional case from the fact that convexity is preserved under composition of functions, if the inner function is convex and the outer function is convex and monotone, and under non-negatively weighted summation or integration [9]. The specific choice of the hyper-parameters in the architecture in the discretized implementation, such as the number of layers, kernel size, etc., is mentioned in the context of the specific experiments in Sec. IV.

C. Learning protocol

Our training strategy follows the one used for training AR [4]. The training protocol is unsupervised, with the dataset consisting of N i.i.d. samples $\{\mathbf{x}_i\}_{i=1}^N \in \mathbb{X}$ and $\{\mathbf{y}_i\}_{i=1}^N \in \mathbb{Y}$ from the marginal distributions π_X and π_Y , respectively. Nevertheless, when the training dataset contains a limited number of examples, we found that training the regularizer using pairs $\{\mathbf{x}_i, \mathcal{A}^\dagger \mathbf{y}_i\}$, where $\mathbf{x}_i \sim \pi_X$ and $\mathbf{y}_i \sim \pi_{\text{data}}(\mathbf{y}_i | \mathbf{x}_i)$, leads to a superior performance as compared to using samples drawn from the marginals. Consequently, although the training paradigm is unsupervised in principle, we approximate the training objective for ACR using paired examples (similarly for AR as well while comparing). The regularizer is trained with the objective of favoring solutions that are similar to true images and penalizing solutions with artifacts, and consequently, it should produce a small output when a true image is given as input and a large output when it is shown an unregularized image. The distribution of unregularized reconstructions is denoted as $\mathcal{A}_\#^\dagger \pi_Y$, the push-forward of π_Y by the pseudo-inverse of the forward operator. Naturally, during training, one seeks to minimize the difference of the average output of \mathcal{R}_θ over the true image distribution π_X and the distribution $\mathcal{A}_\#^\dagger \pi_Y$ of unregularized solutions:

$$\begin{aligned} \theta^* &= \arg \min_{\theta} \left(\mathbb{E}_{\pi_X} [\mathcal{R}_\theta(X)] - \mathbb{E}_{\mathcal{A}_\#^\dagger \pi_Y} [\mathcal{R}_\theta(X)] \right) \\ &\text{subject to } \mathcal{R}_\theta \in 1 - \text{Lipschitz}. \end{aligned} \quad (21)$$

The 1-Lipschitz condition in (21) encourages the output of \mathcal{R}_θ to transition smoothly with respect to the input, thus making the corresponding variational loss stable. The 1-Lipschitz constraint is enforced by adding a gradient-penalty term [10] of the form

$$\mathcal{L}_{\text{gp}} = \lambda_{\text{gp}} \mathbb{E}_{\pi_{X_\epsilon}} \left[(\|\nabla \mathcal{R}_\theta(X_\epsilon)\|_2 - 1)^2 \right], \quad (22)$$

to the training objective in (21), where X_ϵ is uniformly sampled from the line between the samples X and $\mathcal{A}^\dagger Y$.

III. CONVERGENCE OF THE SUBGRADIENT ALGORITHM

Although the regularizer is strongly-convex, it seems exceedingly difficult to come up with a closed-form expression for its proximal operator [11], thus preventing the use of proximal gradient-descent. We, however, show that a sub-gradient descent algorithm converges to the minimizer of the variational loss. We begin by rewriting the variational loss defined in (8) as

$$J_\alpha(\mathbf{x}; \mathbf{y}) = f_\alpha(\mathbf{x}; \mathbf{y}) + \alpha g(\mathbf{x}), \quad (23)$$

where $f_\alpha(\mathbf{x}; \mathbf{y}) = \|\mathcal{A}(\mathbf{x}) - \mathbf{y}\|_{\mathbb{Y}}^2 + \alpha \rho_0 \|\mathbf{x}\|_{\mathbb{X}}^2$ is smooth, strongly-convex, and differentiable, while $g(\mathbf{x}) = \mathcal{R}'(\mathbf{x})$ is convex and 1-Lipschitz. Note that g need not be differentiable. For brevity of notation, we drop the subscript α in the loss functions and denote the Lipschitz constant of g by L_g for generality in the remainder of this section. Since the forward operator is linear, $\nabla f(\cdot; \mathbf{y})$ is Lipschitz-continuous, with a Lipschitz constant which we denote as $L_{\nabla f}$.

The following lemma confirms the existence of a step-size parameter that leads to a convergent subgradient algorithm. Nevertheless, in practice, we found that an appropriately chosen constant step-size works reasonably well. Notably, the standard

sublinear convergence of subgradient updates [12, Sec. 3] is not applicable in our case since the variational objective $J(\cdot; \mathbf{y})$ is not Lipschitz-continuous.

Lemma 1. (*Convergence of subgradient updates*) *Starting from any initial estimate \mathbf{x}_0 , there exist optimal step-sizes*

$$\eta_k^* = 2\alpha\rho_0 \frac{\|\mathbf{x}_k - \hat{\mathbf{x}}\|_{\mathbb{X}}^2}{\|\mathbf{z}_k\|_{\mathbb{X}}^2}$$

such that the updates $\mathbf{x}_{k+1} = \mathbf{x}_k - \eta_k^ \mathbf{z}_k$, where $\mathbf{z}_k = \nabla f(\mathbf{x}_k; \mathbf{y}) + \mathbf{u}_k$, with $\mathbf{u}_k \in \partial(\alpha g(\mathbf{x}_k))$, converge to the minimizer $\hat{\mathbf{x}}$ of $J_\alpha(\mathbf{x}; \cdot)$ defined in (23), i.e., $\lim_{k \rightarrow \infty} \mathbf{x}_k = \hat{\mathbf{x}}$ in \mathbb{X} with respect to the norm topology.*

Proof: Let $e_k = \|\mathbf{x}_k - \mathbf{x}^*\|_{\mathbb{X}}^2$ be the squared estimation error in the k^{th} iteration, and let $\mu = 2\alpha\rho_0$. Omitting the argument \mathbf{y} in $J(\mathbf{x}; \mathbf{y})$ for simplicity and using μ -strong convexity of $J(\mathbf{x})$, we have

$$J(\mathbf{x}_k) \leq J(\mathbf{x}^*) + \langle \mathbf{z}_k, \mathbf{x}_k - \hat{\mathbf{x}} \rangle - \frac{\mu}{2} \|\mathbf{x}_k - \hat{\mathbf{x}}\|_{\mathbb{X}}^2. \quad (24)$$

From Proposition 1, we get $J(\mathbf{x}_k) - J(\mathbf{x}^*) \geq \frac{\mu}{2} \|\mathbf{x}_k - \hat{\mathbf{x}}\|_{\mathbb{X}}^2$, which, combined with (24), leads to

$$\langle \mathbf{z}_k, \mathbf{x}_k - \hat{\mathbf{x}} \rangle \geq \mu \|\mathbf{x}_k - \hat{\mathbf{x}}\|_{\mathbb{X}}^2.$$

Therefore, we have the following bound on e_{k+1} :

$$\begin{aligned} e_{k+1} &= \|\mathbf{x}_{k+1} - \hat{\mathbf{x}}\|_{\mathbb{X}}^2 = \|\mathbf{x}_k - \eta_k \mathbf{z}_k - \hat{\mathbf{x}}\|_{\mathbb{X}}^2 \\ &= \|\mathbf{x}_k - \hat{\mathbf{x}}\|_{\mathbb{X}}^2 - 2\eta_k \langle \mathbf{z}_k, \mathbf{x}_k - \hat{\mathbf{x}} \rangle + \eta_k^2 \|\mathbf{z}_k\|_{\mathbb{X}}^2 \\ &\leq (1 - 2\mu\eta_k) e_k + \eta_k^2 \|\mathbf{z}_k\|_{\mathbb{X}}^2. \end{aligned} \quad (25)$$

The bound in (25) becomes the tightest when

$$\eta_k = \eta_k^* = \frac{\mu e_k}{\|\mathbf{z}_k\|_{\mathbb{X}}^2} = \mu \frac{\|\mathbf{x}_k - \hat{\mathbf{x}}\|_{\mathbb{X}}^2}{\|\mathbf{z}_k\|_{\mathbb{X}}^2},$$

leading to $e_{k+1} \leq e_k - \frac{\mu^2 e_k^2}{\|\mathbf{z}_k\|_{\mathbb{X}}^2}$. This indicates that the estimation error decreases monotonically with iteration. Further, $\|\mathbf{z}_k\|_{\mathbb{X}}^2$ can be bounded as

$$\begin{aligned} \|\mathbf{z}_k\|_{\mathbb{X}}^2 &= \|\nabla f(\mathbf{x}_k) + \mathbf{u}_k\|_{\mathbb{X}}^2 \leq 2 \|\nabla f(\mathbf{x}_k)\|_{\mathbb{X}}^2 + 2 \|\mathbf{u}_k\|_{\mathbb{X}}^2 \\ &\leq 2 \|\nabla f(\mathbf{x}_k)\|_{\mathbb{X}}^2 + 2\alpha^2 L_g^2, \end{aligned} \quad (26)$$

as g is L_g -Lipschitz. Since $\hat{\mathbf{x}}$ is the unique minimizer of $J(\mathbf{x})$, $\exists \hat{\mathbf{u}} \in \partial(\alpha g(\hat{\mathbf{x}}))$ such that $\nabla f(\hat{\mathbf{x}}) + \hat{\mathbf{u}} = 0$. Using the triangle inequality and Lipschitz-continuity of $\nabla f(\mathbf{x})$,

$$\begin{aligned} \|\nabla f(\mathbf{x}_k)\|_{\mathbb{X}} - \|\hat{\mathbf{u}}\|_{\mathbb{X}} &\leq \|\nabla f(\mathbf{x}_k) + \hat{\mathbf{u}}\|_{\mathbb{X}} \\ &= \|\nabla f(\mathbf{x}_k) - \nabla f(\hat{\mathbf{x}})\|_{\mathbb{X}} \\ &\leq L_{\nabla f} \|\mathbf{x}_k - \hat{\mathbf{x}}\|_{\mathbb{X}}, \end{aligned} \quad (27)$$

leading to $\|\nabla f(\mathbf{x}_k)\|_{\mathbb{X}} \leq L_{\nabla f} \sqrt{e_k} + \alpha L_g$. Plugging this in (26) and substituting $\|\mathbf{z}_k\|_{\mathbb{X}}^2$ in (25) with its resulting upper bound, we arrive at

$$e_{k+1} \leq e_k - \frac{\mu^2 e_k^2}{2L_{\nabla f}^2 e_k + 4\alpha L_g L_{\nabla f} \sqrt{e_k} + 4\alpha^2 L_g^2}. \quad (28)$$

methods	optimizer	α	# iterations
AR	gradient-descent, $\eta = 0.5$	0.1	600
ACR	gradient-descent, $\eta = 0.8$	0.05	400

TABLE I
THE OPTIMIZER SETTING FOR THE VARIATIONAL RECONSTRUCTION PROBLEMS CORRESPONDING TO AR AND ACR.

Finally, since $0 \leq e_{k+1} < e_k$, $\lim_{k \rightarrow \infty} e_k$ exists. Denote the limit by e . Taking limit as $k \rightarrow \infty$ on both sides of (28), we get

$$e \leq e - \frac{\mu^2 e}{2L_{\nabla f}^2 e + 4\alpha L_g L_{\nabla f} \sqrt{e} + 4\alpha^2 L_g^2}, \quad (29)$$

implying that $e = 0$ and therefore proving convergence. ■

IV. NUMERICAL RESULTS

For performance evaluation and comparison with the state-of-the-art, we consider three applications, namely, CT reconstruction with (i) sparse- and (ii) limited-view acquisitions, and (iii) natural image deblurring. For the CT experiments, human abdominal CT scans are used for 10 patients provided by Mayo Clinic for the low-dose CT grand challenge [13]. We simulate the projection data by using ODL [14] with the *astra_gpu* backend. Our training dataset for the CT experiments consists of a total of 2250 slices, each of dimension 512×512 , corresponding to 9 patients. The remaining 128 slices corresponding to one patient are used to evaluate the reconstruction performance. The deblurring experiments are conducted on the *STL10* dataset [15]. In all cases, we measure the performance in terms of the peak signal-to-noise ratio (PSNR) and the structural similarity index (SSIM). In all settings, we compare our results also with TV reconstructions, computed by employing the *alternating directions method of multipliers* (ADMM)-based solver in ODL. We choose the penalty parameter of each variational method to maximize the mean PSNR of its reconstructions. Besides the parametrization of ACR elucidated in Sec. II-B, we compare the performance of three simple variants of it. First, we incorporate an additional term of the form

$$\mathcal{R}'_{\text{sfb}}(\mathbf{x}) = \|\mathcal{U}\mathbf{x}\|_1, \quad (30)$$

where \mathcal{U} denotes a two-dimensional convolutional layer, into the regularizer. When the filters in \mathcal{U} have bounded norms, this additional term is also convex and Lipschitz-continuous, like $\mathcal{R}'(\mathbf{x})$. We refer to this term as *sparsifying filter-bank* (SFB) penalty, since the ℓ_1 penalty on $\mathcal{U}\mathbf{x}$ is tantamount to seeking sparsity of \mathbf{x} in the learned filters \mathcal{U} . This additional term is motivated by the widely used wavelet-sparsity prior in image processing and essentially gives ACR a chance to learn a similar prior, and possibly a better one, during training. We compare the performance of all three variants of ACR, namely with (i) $\mathcal{R}'(\mathbf{x})$ and (ii) $\mathcal{R}'(\mathbf{x}) + \mathcal{R}'_{\text{sfb}}(\mathbf{x})$ as the Lipschitz convex part, and (iii) $\mathcal{R}'_{\text{sfb}}(\mathbf{x}) = \|\mathcal{U}\mathbf{x}\|_1$ as the standalone Lipschitz-convex part to investigate if a simpler and more commonly used convex model indeed works on par or better than the ICNN model in Sec. II-B. For all of these variants of ACR, the same training strategy is adopted, as described in Sec. II-C.

The individual details of the experimental setups for all three applications are described in the following.

A. Reconstruction in sparse-view CT

The sparse-view projection data is simulated in ODL using a parallel-beam acquisition geometry with 200 angles and 400 rays/angle. White Gaussian noise with $\sigma = 2.0$ is added to the projection data and used in our experiments. The proposed ACR approach is compared with two model-based techniques, namely filtered back-projection (FBP) and total-variation (TV) regularization, and two data-driven methods, namely the learned primal-dual (LPD) method proposed in [3] and the adversarial regularization (AR) approach [4]. The LPD method is trained on paired examples, while AR and the proposed ACR method are trained in an unsupervised manner.

For LPD and AR, we develop *PyTorch* [16] implementations¹ based on their publicly available *TensorFlow* codes². The optimizer setting used for AR and ACR while solving the variational problem is presented in Table I. The hyper-parameters in Table I are chosen empirically to get the best reconstruction PSNR for our experiments.

The ACR architecture is constructed as described in Sec. II-B with $L = 10$ layers. \mathcal{B}_i and \mathcal{W}_i are convolutional layers with 5×5 kernels applied with a stride of 1 and consisting of 48 output channels. The layers \mathcal{B}_i are restricted to have non-negative weights to preserve convexity, while no such restriction is needed on \mathcal{W}_i 's. The activation at all layers except the final layer is chosen as the leaky-ReLU function with a negative slope of 0.2. The activation of the final layer is the identity function, and we apply a global average pooling on the output feature map to convert it to a scalar. The SFB term is composed of 10 2D convolution layers, each consisting of 7×7 filters with 32 output channels. The *Adam* optimizer [17] is used for training the network, with a learning rate of 2×10^{-5} and $(\beta_1, \beta_2) = (0.5, 0.99)$. The gradient penalty term in (22) is chosen to be 5.0. The penalty parameter ρ_0 corresponding to the squared- ℓ_2 term in ACR is initialized at $\rho_0 = \log(1 + \exp(-9.0))$ and learned from data. ACR and AR were trained for 5 and 10 epochs, respectively. We found that the performance of AR during reconstruction tends to deteriorate if the network is over-trained, while for ACR, we did not find any noticeable improvement or deterioration due to over-training, suggesting that AR is more susceptible to overfitting as compared to ACR.

The performance of ACR and the competing model- and data-based techniques, averaged over the test data, is reported in Table II. Representative reconstructed images for different methods are shown in Fig. 1. The average PSNR and SSIM of the reconstructed images indicate that the proposed ACR method leads to better reconstruction than TV (approximately 1 dB higher PSNR), which is by far the most popular analytical convex regularizer with well-studied convergence properties. Including the SFB term in conjunction with \mathcal{R}' leads to slight improvement in performance, although the SFB term alone

¹The ACR implementation is available upon request.

²LPD: https://github.com/adler-j/learned_primal_dual, AR: <https://github.com/lunz-s/DeepAdversarialRegulariser>

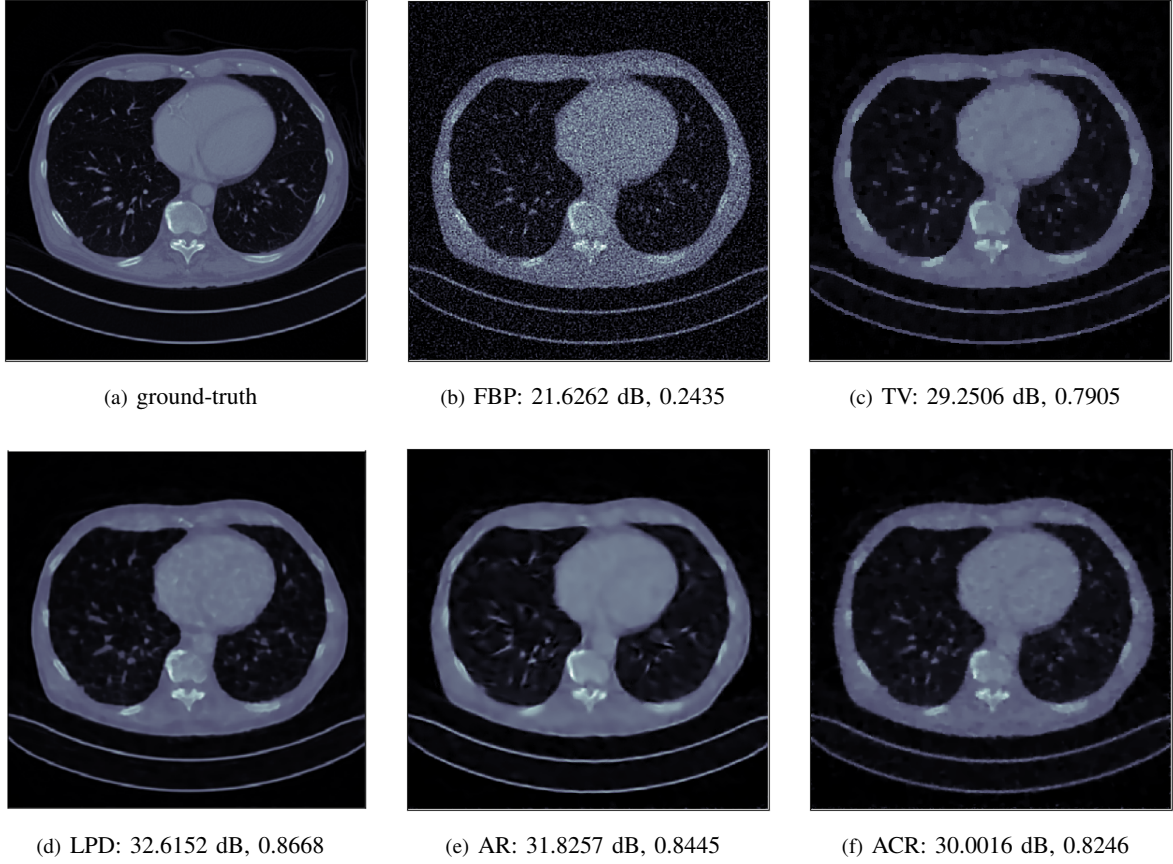


Fig. 1. Comparison of different reconstruction methods for sparse-view CT. The learned ACR approach outperforms the most widely used TV-based convex regularization. AR turns out to be better than ACR in this case, pointing to the limited expressive power of a convex regularizer. LPD trained on supervised data leads to the best performance.

methods	PSNR (dB)	SSIM	# parameters
FBP	21.2866	0.2043	1
TV	30.3476	0.8110	1
LPD	34.3590	0.8889	411680
AR	33.6207	0.8750	19347890
ACR (no SFB)	31.2822	0.8468	590928
ACR (with SFB)	31.4555	0.8644	606609
$SFB + \rho_0 \ \mathbf{x}\ _2^2$	26.8001	0.5678	15681

TABLE II
AVERAGE PSNR AND SSIM OVER TEST DATA FOR DIFFERENT RECONSTRUCTION METHODS FOR SPARSE-VIEW CT.

turns out to be significantly inferior to TV. This indicates the need for a convex regularizer, like ours, that goes beyond linear sparsity-based convex prior models and learns more intricate structures specific to the application at hand. For the sparse-view CT experiment, the classical AR approach yields reconstruction that is superior to ACR, although our experiments in the sequel reveal that this improvement is not consistent across applications. As one would expect, the LPD framework trained using paired examples performs the best among all the methods we compare.

B. Reconstruction in limited-angle CT

CT reconstruction from limited-angle projection data, where no measurement is available in a particular angular region, is considered as a particularly challenging ill-posed inverse problem. Limited-angle projections arise primarily because of limited scan-time or restricted scanner movement in certain applications. Due to the lack of projection data in an angular region, the reconstruction performance depends critically on the image prior. Akin to the sparse-view CT experiment, the data for the limited-angle CT experiment is generated using ODL with a parallel-beam acquisition geometry. The projection data is corrupted using white Gaussian noise with $\sigma = 3.2$ and reconstructed with 350 angles, 700 rays/angle, with a missing angular wedge of 60° . In this experiment, we compare our method with two model-based (FBP and TV as before) and two data-driven approaches, namely, a U-net [18] based denoiser and AR. The U-net denoiser is trained in a supervised manner, with the FBP reconstruction as the input and the true image as the target, similar to the post-processing approach followed in [19]. We found that unlike sparse-view CT, such a post-processing network works better than the LPD method for limited-angle CT.

The ACR architecture is constructed with $L = 5$ layers, and \mathcal{B}_i and \mathcal{W}_i are all chosen as convolutional layers with 5×5 kernels

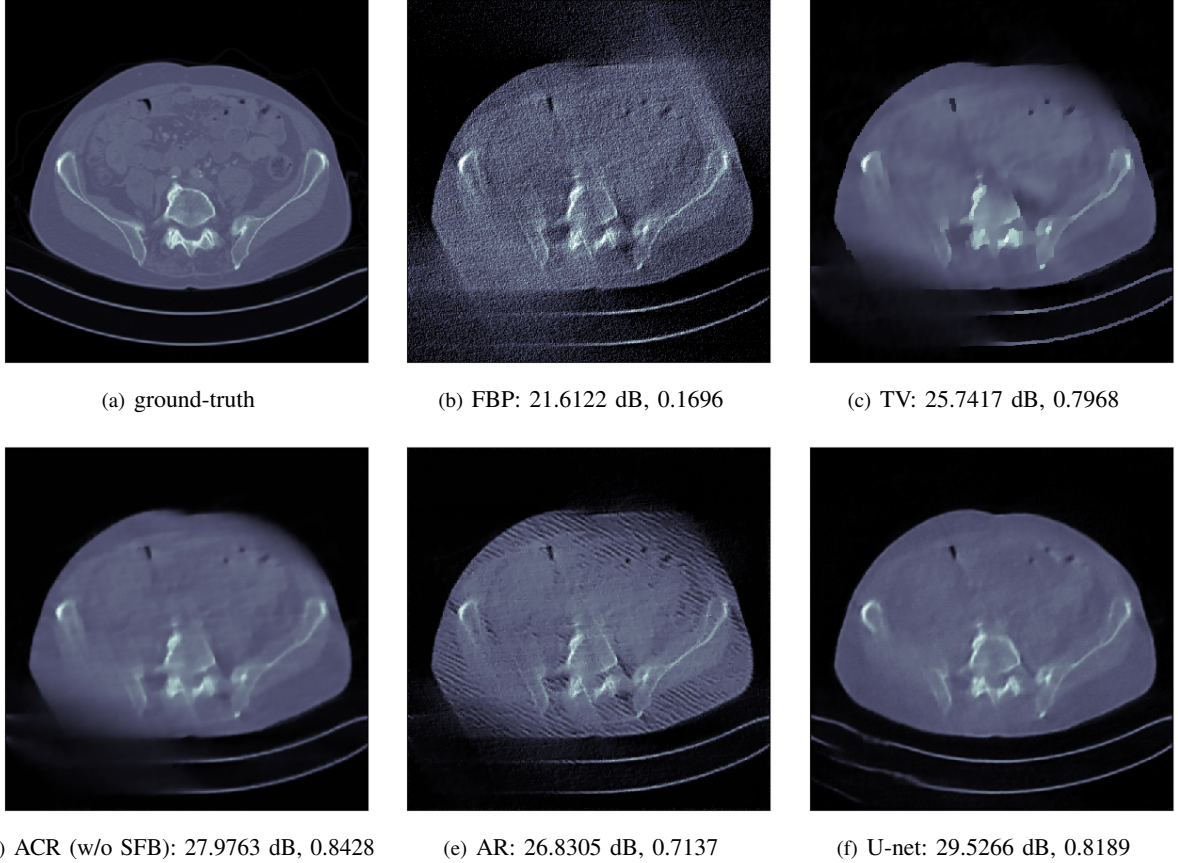


Fig. 2. Reconstructed images obtained using different methods, along with the associated PSNR and SSIM, for limited-angle CT. In this case, ACR outperforms TV and AR in terms of reconstruction quality.

and 16 channels. The *RMSprop* optimizer with a learning rate of 5×10^{-5} is used for training. The gradient penalty term in (22) is chosen to be 10.0 and the penalty parameter ρ_0 is initialized the same way as in the sparse-view CT experiment. The convolutional layers for the SFB is taken as 5×5 filters with 32 output channels.

The reconstruction is done by solving the variational problem via gradient-descent for 2000 iterations with step size of 10^{-5} . We observed that the reconstruction performance of AR can deteriorate if an early stopping is not applied. So, for a fair comparison, we report the highest PSNR achieved by AR during reconstruction, while such an early stopping was not needed for ACR. This phenomenon indicates the algorithmic advantage of a convex regularizer over a non-convex one.

The average PSNR and SSIM are reported in Table III for various competing methods. To facilitate visual comparison, an example of the reconstruction quality for a representative test image is provided in Fig. 2. From the average PSNR and SSIM reported in Table III, we can see that ACR outperforms both model-based approaches and AR. As opposed to sparse-view CT, AR under-performs significantly in the limited-angle case and produces streak-like artifacts that cover the whole image and are particularly concentrated near the missing angular regions. One of the reasons for this behaviour is because of a rather small training dataset, which leads to the AR model overfitting to the training data. This problem does not arise

methods	PSNR (dB)	SSIM	# parameters
FBP	15.7418	0.0920	1
TV	25.6778	0.7934	1
SFB	19.1876	0.1436	8 001
AR	23.6475	0.6257	133 792
ACR (no SFB)	26.4459	0.8184	34 897
ACR (with SFB)	26.7767	0.8266	42 898
U-net denoiser	29.0308	0.8002	14 787 777

TABLE III
AVERAGE PSNR AND SSIM OVER TEST DATA FOR DIFFERENT RECONSTRUCTION METHODS FOR LIMITED-ANGLE CT.

in case of ACR, which, thanks to lower model capacity, can successfully evade the peril of overfitting when the amount of training data is limited. Thus, contrary to the conventional intuition, the restricted expressive power of a convex regularizer turns out to be advantageous, especially in a limited data scenario with a highly ill-conditioned forward operator. Similar to sparse-view CT, including the SFB term in ACR leads to a slightly better reconstruction performance and the SFB term as the standalone convex regularizer performs worse than both TV and ACR with and without the SFB term.

methods	TV	SFB	ACR	AR	AR2
# parameters	1	4 706	142 594	2 562 242	142 594

TABLE IV
NUMBER OF PARAMETERS IN EACH OF THE DEBLURRING METHODS.

C. Image deblurring

We will now describe the experimental setup and numerical results for the image deblurring task conducted on the STL10 dataset [15]. The deblurring dataset is created by computing the noisy measurements, \mathbf{y}^δ , by first smoothing the ground truth images, $\mathbf{x} \in [0, 1]^{3 \times 96 \times 96}$, from the STL10 dataset, with a 3×3 averaging filter in each of the RGB channels and subsequently adding zero-centered Gaussian noise with a standard deviation of 0.05. All variants of AR and ACR are trained on pairs $(\mathbf{x}_i, \mathcal{A}^\dagger \mathbf{y}_i^\delta)$, where we approximated the action of \mathcal{A}^\dagger on the measurement via an overfitting Landweber reconstruction, i.e., by stopping it past the Morozov's principle.

The architecture of the Lipschitz-convex component \mathcal{R}' in ACR is a discretized version of the architecture described to Section II-B and is built by $L = 5$ layers. We set φ_i to be the leaky-ReLU function with a negative slope of 0.2 for $i = 0, \dots, L-1$. For the final layer we set, φ_L to be an identity mapping. All \mathcal{B}_i and \mathcal{W}_i are given by convolutional layers with kernels of size 5×5 and 32 output channels. The dimensional reduction to a single real-valued output in the last layer occurs via a mean pooling. The weights of the \mathcal{B}_i 's are projected to be non-negative after each training step to preserve convexity. The convolutional layer in the SFB consists of a 7×7 kernel and has 32 output channels. We compare the ACR and the SFB with the original AR and, due to its slightly sub-optimal performance, a second adversarial regularizer which we refer to as AR2. The AR2 regularizer has the same architecture as the ACR, but the \mathcal{B}_i 's are not restricted to be non-negative, thus allowing it to be non-convex. AR2 has significantly fewer parameters than AR and is less prone to overfitting as a consequence.

All models are trained for 8 epochs with a batch size of 100 using the *Adam* optimizer with a learning rate of $5 \cdot 10^{-5}$ and $\beta = (0.9, 0.99)$. The number of trainable parameters in the networks are given in Table IV. Subsequent to training, we compute the reconstructions by minimizing the corresponding variational functional. The optimization is carried out by using gradient descent for 4096 steps with a step size of $10^4/27648 \approx 0.36$ (27648 is the size of the image/measurement). We chose the best reconstruction out of all the 4096 steps, which (with the PSNR maximizing penalty parameter) was, in all cases, approximately the last iteration.

The results of the experiments are reported in Table V along with representative reconstructions. One can see that all learned reconstruction methods outperform TV. However, while the ACR and the AR2 outperform TV by a significant margin, e.g., approximately 1 dB for the PSNR values, AR only outperforms it by a somewhat smaller margin, and the SFB only outperforms TV by half a dB. The results lead us to two conclusions for this deblurring setting: (i) The convexity of the ACR does not seem to be a significant constraint in terms of performance, and (ii) one seems to benefit from using more powerful convex

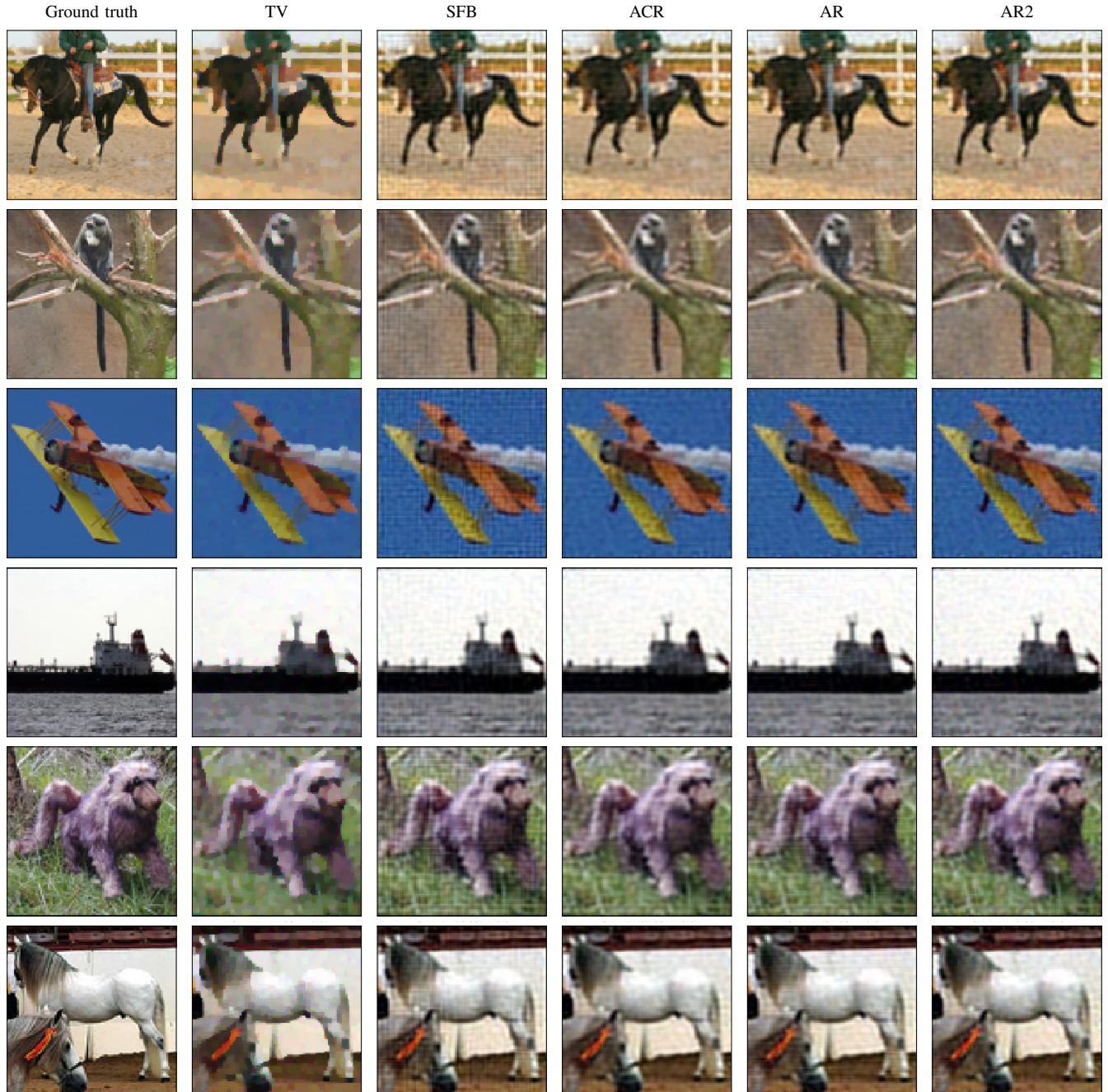
models than the SFB.

V. CONCLUSIONS

We proposed a novel data-driven strongly-convex regularization approach for inverse problems and established analytical convergence guarantee and stability estimate. Moreover, we showed the existence of a sub-gradient descent algorithm for minimizing the variational loss, leading to a reconstruction error that decays to zero with iterations. The proposed ACR approach brings together the power of data-driven inference and the provability of analytical convex regularization. Numerical performance evaluation on sparse-view CT suggests that ACR is superior to the classical TV reconstruction, but gets outperformed by the non-convex AR method, albeit with significantly fewer parameters in the regularizer network as compared to AR. The image deblurring experiment indicates that the ACR model is at least on par and sometimes better than AR in terms of reconstruction quality, thus showing clear advantage both in terms of theoretical guarantees and numerical performance. We also noted that ACR could be parametrized more parsimoniously as compared to its non-convex counterpart without significantly affecting the performance, while avoiding overfitting in a limited-data scenario.

REFERENCES

- [1] S. Arridge, P. Maass, O. Öktem, and C.-B. Schönlieb, "Solving inverse problems using data-driven models," *Acta Numerica*, vol. 28, pp. 1–174, 2019.
- [2] J. Adler and O. Öktem, "Solving ill-posed inverse problems using iterative deep neural networks," *Inverse Problems*, vol. 33, no. 12, 2009.
- [3] J. Adler and O. Öktem, "Learned primal-dual reconstruction," *IEEE transactions on medical imaging*, vol. 37, no. 6, pp. 1322–1332, 2018.
- [4] S. Lunz, O. Öktem, and C.-B. Schönlieb, "Adversarial regularizers in inverse problems," in *Advances in Neural Information Processing Systems*, 2018, pp. 8507–8516.
- [5] H. Li, J. Schwab, S. Antholzer, and M. Haltmeier, "Nett: Solving inverse problems with deep neural networks," *arXiv preprint arXiv:1803.00092v3*, Dec. 2019.
- [6] B. Amos, L. Xu, and J. Z. Kolter, "Input convex neural networks," in *International Conference on Machine Learning*, 2017, pp. 146–155.
- [7] P. Peng, S. Jalali, and X. Yuan, "Auto-encoders for compressed sensing," 2019.
- [8] S. Dittmer, T. Kluth, P. Maass, and D. O. Baguer, "Regularization by architecture: A deep prior approach for inverse problems," *Journal of Mathematical Imaging and Vision*, pp. 1–15, 2019.
- [9] S. Boyd, S. P. Boyd, and L. Vandenberghe, *Convex optimization*. Cambridge university press, 2004.
- [10] I. Gulrajani1, F. Ahmed, M. Arjovsky, V. Dumoulin, and A. Courville, "Improved training of wasserstein gans," *arXiv preprint arXiv:1704.00028v3*, Dec. 2017.
- [11] N. Parikh and S. Boyd, "Proximal algorithms," *Foundations and Trends in optimization*, vol. 1, no. 3, pp. 127–239, 2014.
- [12] S. Boyd, *Subgradient methods*, May 2014 (accessed July 27, 2020). [Online]. Available: https://stanford.edu/class/ee364b/lectures/subgrad_method_notes.pdf
- [13] C. McCollough, "Tfg-207a-04: Overview of the low dose ct grand challenge," *Medical Physics*, vol. 43, no. 6, pp. 3759–3760, 2014.
- [14] J. Adler, H. Kohr, and O. Öktem, "Operator discretization library (odl)," *Software available from https://github.com/odlgroup/odl*, 2017.
- [15] A. Coates, A. Ng, and H. Lee, "An analysis of single-layer networks in unsupervised feature learning," in *Proceedings of the fourteenth international conference on artificial intelligence and statistics*, 2011, pp. 215–223.
- [16] A. Paszke, S. Gross, S. Chintala, G. Chanan, E. Yang, Z. DeVito, Z. Lin, A. Desmaison, L. Antiga, and A. Lerer, "Automatic differentiation in pytorch," 2017.
- [17] D. P. Kingma and J. Ba, "Adam: A method for stochastic optimization," *arXiv preprint arXiv:1412.6980*, 2014.



PSNR stats:	mean: 25.50 median: 25.01 std. div.: 2.08	mean: 26.05 median: 25.82 std. div.: 1.71	mean: 26.55 median: 26.12 std. div.: 2.05	mean: 26.35 median: 25.99 std. div.: 1.98	mean: 26.57 median: 26.21 std. div.: 1.88
SSIM stats:	mean: 0.80 median: 0.80 std. div.: 0.05	mean: 0.81 median: 0.81 std. div.: 0.04	mean: 0.83 median: 0.83 std. div.: 0.03	mean: 0.82 median: 0.82 std. div.: 0.03	mean: 0.83 median: 0.83 std. div.: 0.03

TABLE V
DEBLURRING OF STL10 IMAGES (STATS OVER 100 SAMPLES).

- [18] O. Ronneberger, P. Fischer, and T. Brox, “U-net: Convolutional networks for biomedical image segmentation,” *Springer International Publishing*, pp. 234–241, 2015.
- [19] K. H. Jin, M. T. McCann, E. Froustey, and M. Unser, “Deep convolutional neural network for inverse problems in imaging,” *IEEE Transactions on Image Processing*, vol. 26, no. 9, pp. 4509–4522, 2017.